

A modified analytical model of the alkali-metal atomic magnetometer employing longitudinal carrier field

Chang Chen(陈畅), Yi Zhang(张燚), Zhi-Guo Wang(汪之国), Qi-Yuan Jiang(江奇渊), Hui Luo(罗晖), Kai-Yong Yang(杨开勇)

Citation: Chin. Phys. B, 2021, 30 (**5**): 050707. DOI: 10.1088/1674-1056/abd7d3
Journal homepage: http://cpb.iphy.ac.cn; http://iopscience.iop.org/cpb

What follows is a list of articles you may be interested in

In-situ fabrication of ZnO nanoparticles sensors based on gas-sensing electrode for ppb-level H_2S detection at room temperature

Jing-Yue Xuan(宣景悦), Guo-Dong Zhao(赵国栋), Xiao-Bo Shi(史小波), Wei Geng(耿伟), Heng-Zheng Li(李恒征), Mei-Ling Sun(孙美玲), Fu-Chao Jia(贾福超), Shu-Gang Tan(谭树刚), Guang-Chao Yin(尹广超), and Bo Liu(刘波)
Chin. Phys. B, 2021, 30 (**2**): 020701. DOI: 10.1088/1674-1056/abcf46

Fiber cladding SPR bending sensor characterized by two parameters

Chunlan Liu(刘春兰), Jiangxi Hu(胡江西), Yong Wei(魏勇), Yudong Su(苏于东), Ping Wu(吴萍), Lingling Li(李玲玲), and Xiaoling Zhao(赵晓玲)
Chin. Phys. B, 2020, 29 (**12**): 120701. DOI: 10.1088/1674-1056/aba9c1

Acetone sensors for non-invasive diagnosis of diabetes based on metal-oxide-semiconductor materials

Yujie Li(李育洁), Min Zhang(张敏), Haiming Zhang(张海明)
Chin. Phys. B, 2020, 29 (**9**): 090702. DOI: 10.1088/1674-1056/aba60b

A synthetic optically pumped gradiometer for magnetocardiography measurements

Shu-Lin Zhang(张树林), Ning Cao(曹宁)
Chin. Phys. B, 2020, 29 (**4**): 040702. DOI: 10.1088/1674-1056/ab7801

Microfluidic temperature sensor based on temperature-dependent dielectric property of liquid

Qi Liu(刘琦), Yu-Feng Yu(俞钰峰), Wen-Sheng Zhao(赵文生), Hui Li(李慧)
Chin. Phys. B, 2020, 29 (**1**): 010701. DOI: 10.1088/1674-1056/ab593c

---

A modified analytical model of the alkali-metal atomic magnetometer employing longitudinal carrier field*

Chang Chen(陈畅)[1,2], Yi Zhang(张燚)[1,2], Zhi-Guo Wang(汪之国)[1,2,†], Qi-Yuan Jiang(江奇渊)[1,2], Hui Luo(罗晖)[1,2], and Kai-Yong Yang(杨开勇)[1,2]

[1] College of Advanced Interdisciplinary Studies, National University of Defense Technology, Changsha 410073, China
[2] Interdisciplinary Center for Quantum Information, National University of Defense Technology, Changsha 410073, China

(Received 9 November 2020; revised manuscript received 18 December 2020; accepted manuscript online 4 January 2021)

Alkali-metal atomic magnetometers employing longitudinal carrier magnetic field have ultrahigh sensitivity to measure transverse magnetic fields and have been applied in a variety of precise-measurement science and technologies. In practice, the magnetometer response is not rigorously proportional to the measured transverse magnetic fields and the existing fundamental analytical model of this magnetometer is effective only when the amplitudes of the measured fields are very small. In this paper, we present a modified analytical model to characterize the practical performance of the magnetometer more definitely. We find out how the longitudinal magnetization of the alkali metal atoms vary with larger transverse fields. The linear-response capacity of the magnetometer is determined by these factors: the amplitude and frequency of the longitudinal carrier field, longitudinal and transverse spin relaxation time of the alkali spins and rotation frequency of the transverse fields. We give a detailed and rigorous theoretical derivation by using the perturbation-iteration method and simulation experiments are conducted to verify the validity and correctness of the proposed modified model. This model can be helpful for measuring larger fields more accurately and configuring a desirable magnetometer with proper linear range.

Keywords: alkali-metal atomic magnetometer, longitudinal carrier magnetic field, linear-response capacity

PACS: 07.07.Df, 07.55.Ge, 42.79.−e **DOI:** 10.1088/1674-1056/abd7d3

1. Introduction

Alkali-metal atomic (AMA) magnetometers[1,2] using parametric modulation can achieve ultrahigh sensitivity in the order of nT–fT, due to the advantages of the synchronous demodulation techniques and suppression of low-frequency flicker noise. They have been demonstrated for the detection of biomagnetic signals from the human body,[3] magnetic resonance imaging (MRI),[4] fundamental physics study,[5] the detection of low-field nuclear magnetic resonance (NMR)[6] and other applications. The AMA magnetometer employing an oscillating carrier magnetic field along the z-axis as the longitudinal direction, was first devised in Ref. [7] and used to detect ^{3}He nuclear polarization.[8] Later, by applying a static magnetic field and optical pumping light along the same direction of the carrier field, this magnetometer technique was developed and used in spin-exchange[9,10] NMR oscillators or gyroscopes,[11,12] as a vector magnetometer that is maximally sensitive to the low-frequency and very weak magnetic fields B_T in the x–y plane caused by the processing nuclear magnetization vector in the alkali vapor cell, and insensitive to B_z along the rotation axis of the gyroscopes.[13]

Following the derivations in Ref. [7], the analytical models presented in Ref. [12] describe the rubidium magnetometer signal that is only proportional to small magnetic fields B_x and B_y within the linewidth of the rubidium magnetization vector, because it is assumed that the longitudinal component of the rubidium magnetization M_z is constant. Reference [14] demonstrated a two-transverse axis atomic magnetometer by utilizing parametric modulation of the z-magnetic field and operating in the spin-exchange relaxation-free regime, under the condition that they also approximated the z-component of the Rb atomic spin polarization S_z is S_0, which is determined by optical pumping and any magnetic-field-induced changes can be neglected. References [12,14] mainly considered the sensitivity of the magnetometer and they have done little research on its linear-response characteristics. Reference [15] demonstrated a three-axis atomic magnetometer employing longitudinal field modulation, which can not only measure the transverse components, but the longitudinal z-component of the external magnetic field, by extraction from the modulation frequency that tracks the resonance frequency. They modified the expression of the quasi-static magnetic field $B_{\rm tot}$ to explain the reducing orthogonality of the magnetometer for larger transverse fields. However, there are considerable differences between their modified theoretical curve and experimental curve of the magnetometer response when B_x and B_y are larger than 100 nT. In practice, we cannot ignore that the

*Project supported by the Hunan Graduate Research and Innovation Project (Grant No. CX2018B009), the Natural Science Foundation of Hunan (Grant No. 2018JJ3608), the Research Project of National University of Defense Technology (Grant Nos. ZK170204 and ZZKY-YX-07-02), and the National Natural Science Foundation of China (Grant Nos. 61671458 and 61701515).

†Corresponding author. E-mail: maxborn@nudt.edu.cn

© 2021 Chinese Physical Society and IOP Publishing Ltd

longitudinal magnetization M_z will be influenced by and vary with the magnetic fields B_T in the x–y plane, especially for a large measuring range.

In this work, we study the problem of how large magnetic fields in the x–y plane influence the longitudinal magnetization M_z and study the linear-measurement characteristics of the magnetometer within a relatively large range of B_T. We give a detailed and rigorous theoretical derivation by using the perturbation-iteration method to obtain a modified analytical model of this magnetometer. The simulation experiment results are presented to verify our theoretical model. This work will help us to find the factors that influence the linear-response capacity of the magnetometer and configure proper working conditions for a practical measuring system.

2. System setup

A schematic of a typical apparatus of this type of AMA magnetometer is shown in Fig. 1. The sample cell made of glass is placed in magnetic shields, containing a few milligrams of alkali metal and some buffer gas or noble gas. The cell is heated by hot air or non-magnetic electronic heaters driven by high-frequency AC currents, to ensure sufficient number density of alkali-metal atoms. The sum of all of the individual alkali spins in the vapor cell can be represented by the macroscopic magnetization vector $\boldsymbol{M} = (M_x, M_y, M_z)$ in the xyz-laboratory coordinate system. Uniform static field and carrier field are applied along the z-axis, $B_z = B_0 + B_c \cos(\omega_c t)$. A beam of strong circularly polarized laser tuned to an atomic resonance is applied to transmit through the vapor cell along the z-axis, to polarize the alkali spins by optical pumping.[16] A beam of weak linearly polarized laser tuned near an atomic resonance is applied to transmit through the vapor cell along the x-axis and detected by a photodetector, to sense the x-component of the alkali spin polarization M_x by the Faraday optical rotation method.[17] The output of the detector is sent to a signal processing system to extract the B_x and B_y information from the modulated signal M_x.

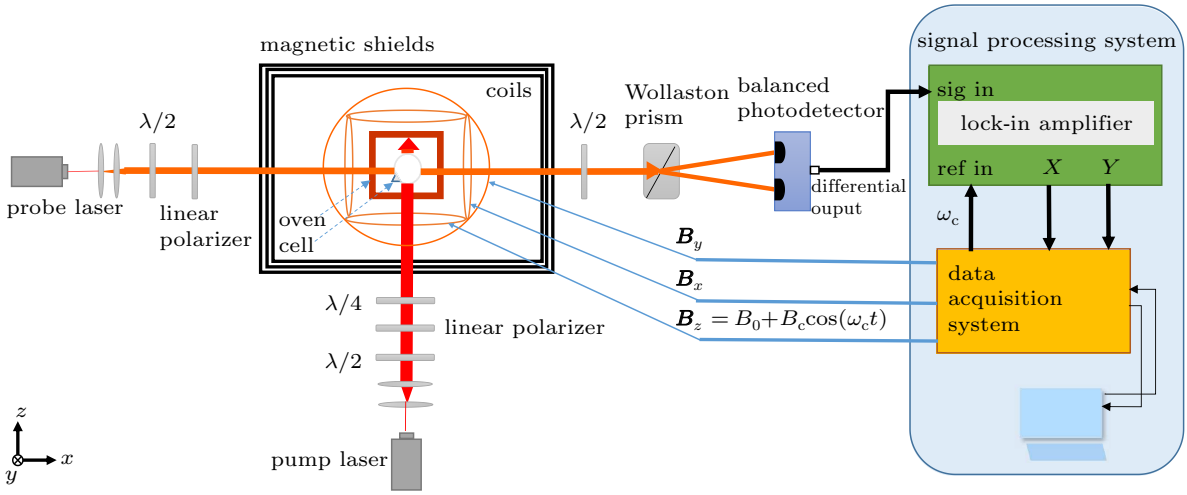


Fig. 1. Schematic of a typical apparatus of an alkali-metal atomic magnetometer employing a longitudinal carrier magnetic field.

3. Theoretical derivation

When the magnetization vector $\boldsymbol{M}$ interacts with the external magnetic fields $\boldsymbol{B} = (B_x, B_y, B_z)$ and the optical pumping light, the dynamics of the magnetization can be described by the Bloch-like equation[7]

$$\frac{\mathrm{d}\boldsymbol{M}}{\mathrm{d}t} = \boldsymbol{M} \times \gamma \boldsymbol{B} - \frac{M_x \boldsymbol{x} + M_y \boldsymbol{y}}{\tau_2} + \frac{M_0 - M_z}{\tau_1} \boldsymbol{z}, \tag{1}$$

where, $\boldsymbol{x}$, $\boldsymbol{y}$ and $\boldsymbol{z}$ are the unit vectors along the x, y and z axis, respectively; γ is the gyro-magnetic ratio of the alkali spin; M_0 is the longitudinal z-component of the magnetization of alkali spins in the equilibrium state when optical pumping is on, τ_1 and τ_2 are the longitudinal relaxation time and the transverse relaxation time of alkali spins, respectively, which are the total time constants that include both the optical pumping and relaxation effects.[18] Under normal conditions, optical pumping is much stronger than the relaxation, and τ_1 and τ_2 are in the order of μs–ms.

Assuming that the slowly varying magnetic fields to be measured are along the x-axis, $B_y = 0$. By setting $M_+ = M_x + \mathrm{i}M_y$, equation (1) now can be written as

$$\frac{\mathrm{d}M_+}{\mathrm{d}t} + \left\{ \frac{1}{\tau_2} + \mathrm{i}\left[\omega_0 + \omega_1 \cos(\omega_c t)\right] \right\} M_+ = \mathrm{i}\gamma B_x M_z, \tag{2a}$$

$$\frac{\mathrm{d}M_z}{\mathrm{d}t} = \frac{[M_0 - \tau_1 \gamma B_x M_y] - M_z}{\tau_1}, \tag{2b}$$

where $\omega_0 = \gamma B_0$ and $\omega_1 = \gamma B_c$.

When $\omega_c \gg 1/\tau_2$ (the frequency of the modulation field is much higher than the spin relaxation rate), magnetization M_+ cannot respond to the modulation field synchronously and will oscillate at various harmonics of modulation frequency ω_c (i.e., M_+ contains high-frequency components).

3.1. The fundamental analytical model

First of all, we give a brief introduction of the existing fundamental model describing the working principle of this type of AMA magnetometer.

When the amplitudes of the measured magnetic fields B_x are much smaller than that of the static field, $|B_x| \ll \frac{1}{\gamma\tau_1} \ll B_0$, then the longitudinal magnetization M_z in Eq. (2b) will very quickly (typically within the time in the order of μs–ms) arrive at a steady-state, which is nearly a constant: M_0, even if B_x is changing. On the other hand, under normal conditions, the frequency of the measured magnetic fields B_x is much lower than modulation frequency ω_c. Hence, the quantity $B_x M_z \approx B_x M_0$ in Eq. (2a) can be treated as a quasi-invariable factor, compared to the modulation fields.

Then, the formal solution of $M_+(t)$ in Eq. (2a) can be written as

$$M_+(t) = \lambda \times \mathrm{e}^{-t/\tau_2}\mathrm{e}^{-\mathrm{i}\left[\omega_0 t + \frac{\omega_1}{\omega_c}\sin(\omega_c t)\right]}, \tag{3}$$

where λ is an unknown expression to be solved later, which should satisfy

$$\frac{\mathrm{d}\lambda}{\mathrm{d}t} = \mathrm{e}^{t/\tau_2}\,\mathrm{e}^{\mathrm{i}\left[\omega_0 t + \frac{\omega_1}{\omega_c}\sin(\omega_c t)\right]} \cdot \mathrm{i}\gamma B_x M_0. \tag{4}$$

Now, we need to obtain the expression of λ by deducing the indefinite integral of Eq. (4). Therefore, we consider transforming $\mathrm{e}^{\mathrm{i}\frac{\omega_1}{\omega_c}\sin(\omega_c t)}$ to be the formalism of Fourier expansion[7]

$$\mathrm{e}^{\pm\mathrm{i}\frac{\omega_1}{\omega_c}\sin(\omega_c t)} = \sum_{n=-\infty}^{n=+\infty} J_n\left(\frac{\omega_1}{\omega_c}\right)\mathrm{e}^{\pm\mathrm{i}n\omega_c t}, \tag{5}$$

where n is an integer and $J_n(x)$ is the Bessel function of order n of the first kind whose argument is $x = \omega_1/\omega_c$, and $J_n(x) = (-1)^n J_{-n}(x)$.

Substituting Eq. (5) into Eq. (4), we solve λ by calculating its indefinite integral. Then, substituting Eq. (5) and the solved expression of λ into Eq. (3), we can obtain the analytic solution to Eq. (2a)

$$M_+ = \mathrm{i}M_0\tau_2\gamma B_x \sum_{p=-\infty}^{+\infty}\sum_{n=-\infty}^{+\infty} \frac{J_n(\beta)J_{n-p}(\beta)}{1+\mathrm{i}\tau_2(\gamma B_0 + n\omega_c)}\mathrm{e}^{\mathrm{i}p\omega_c t}, \tag{6}$$

where p is an integer.

The modulation part δM_x of $M_x = \mathrm{Re}[M_+]$ can be obtained as

$$\begin{aligned}\delta M_x = {} & M_0\tau_2\gamma\sum_{p=1}^{\infty}\left[\sum_{n=-\infty}^{+\infty}\frac{\beta_{np}^-}{1+\tau_2^2(\omega_0+n\omega_c)^2}\right]B_x\sin p\omega_c t \\ & + \left[\sum_{n=-\infty}^{+\infty}\frac{\beta_{np}^+\cdot\tau_2(\omega_0+n\omega_c)}{1+\tau_2^2(\omega_0+n\omega_c)^2}\right]B_x\cos p\omega_c t,\end{aligned} \tag{7a}$$

where

$$\beta_{np}^- = J_n\left(\frac{\omega_1}{\omega_c}\right)\left[J_{n+p}\left(\frac{\omega_1}{\omega_c}\right) - J_{n-p}\left(\frac{\omega_1}{\omega_c}\right)\right], \tag{7b}$$

$$\beta_{np}^+ = J_n\left(\frac{\omega_1}{\omega_c}\right)\left[J_{n+p}\left(\frac{\omega_1}{\omega_c}\right) + J_{n-p}\left(\frac{\omega_1}{\omega_c}\right)\right]. \tag{7c}$$

It can be seen that M_x is composed of the various harmonics of modulation, where each signal of $p\omega_c$ resonates at $\omega_0 + n\omega_c = 0$ and the width is $\Delta\omega_0 = 2/\tau_2$.

The fundamental model describing the magnetometer signal given by Eq. (7a) shows that, under the condition that the amplitude of the measured magnetic field B_x is very small, the longitudinal magnetization $M_z \approx M_0$. Therefore, the amplitude of the magnetometer signal δM_x is proportional to the magnetic fields B_x. Hence, B_x can be extracted from the δM_x signal by in-phase or quadrature demodulation at harmonic $p\omega_c$.

3.2. The modified analytical model

Now, we apply the perturbation-iteration method to solve Eqs. (2a) and (2b). Assuming that M_+ and M_z can be expanded as a power series of B_x, let

$$M_+ = A + B\cdot B_x + C\cdot B_x^2 + D\cdot B_x^3 + \cdots, \tag{8a}$$

$$M_z = Q + E\cdot B_x + F\cdot B_x^2 + G\cdot B_x^3 + \cdots, \tag{8b}$$

where B_x is the pertabation; A, B, C, D, Q, E, F,G,... represent unknown expressions to be solved later; the expression $A + B\cdot B_x + C\cdot B_x^2 + \cdots + X\cdot B_x^q$ is defined as the approximated analytical solution for M_+ of order q; the expression $Q + E\cdot B_x + F\cdot B_x^2 + \cdots + Y\cdot B_x^q$ is defined as the approximated analytical solution for M_z of order q.

3.2.1. Derivation of $M_z^{(0)}$, the solution for M_z of order $q = 0$

In Eq. (2b), let $B_x = 0$, and we have

$$\frac{\mathrm{d}M_z^{(0)}}{\mathrm{d}t} = \frac{M_0 - M_z^{(0)}}{\tau_1}. \tag{9}$$

We consider the steady-state solution, setting Eq. (9) equal to zero, and we obtain

$$M_z^{(0)} = M_0. \tag{10}$$

$M_z^{(0)}$ will very quickly (typically within the time in the order of μs–ms) arrive to and keep staying at the steady-state M_0.

3.2.2. Derivation of $M_+^{(1)}$, the solution for M_+ of order $q = 1$

Substituting $M_z^{(0)}$ of Eq. (10) into Eq. (2a), Eq. (2a) can be written as

$$\frac{\mathrm{d}M_+^{(1)}}{\mathrm{d}t} + \left[\frac{1}{\tau_2} + \mathrm{i}\omega_0 + \mathrm{i}\omega_1\cos(\omega_c t)\right]M_+^{(1)} = \mathrm{i}M_z^{(0)}\gamma B_x. \tag{11}$$

For the same reason as in Subsection 3.1, the quantity $M_z^{(0)}B_x$ in Eq. (11) can be treated as a constant quantity compared to the modulation fields. Under these conditions, by the same method as in Subsection 3.1, we can obtain the analytical

solution to Eq. (11)

$$M_+^{(1)} = \mathrm{i} M_z^{(0)} \tau_2 \gamma B_x \sum_{p=-\infty}^{+\infty} \sum_{n=-\infty}^{+\infty} \frac{J_n\left(\frac{\omega_1}{\omega_c}\right) J_{n-p}\left(\frac{\omega_1}{\omega_c}\right)}{1+\mathrm{i}\tau_2\left(\gamma B_0 + n\omega_c\right)} \mathrm{e}^{\mathrm{i}p\omega_c t}. \quad (12)$$

Then, we can obtain $M_y^{(1)} = \mathrm{Im}\left[M_+^{(1)}\right]$,

$$\begin{aligned} M_y^{(1)} = {} & M_z^{(0)} \tau_2 \gamma B_x \cdot \sum_{n=-\infty}^{n=+\infty} \frac{J_n^2\left(\frac{\omega_1}{\omega_c}\right)}{1+\tau_2^2\left(\omega_0 + n\omega_c\right)^2} \\ & + M_z^{(0)} \tau_2 \gamma \sum_{p=1}^{\infty} \left[\sum_{n=-\infty}^{n=+\infty} \frac{\beta_{np}^+}{1+\tau_2^2\left(\omega_0+n\omega_c\right)^2}\right] B_x \cos p\omega_c t \\ & + \left[\sum_{n=-\infty}^{n=+\infty} \frac{-\beta_{np}^- \cdot \tau_2\left(\omega_0 + n\omega_c\right)}{1+\tau_2^2\left(\omega_0+n\omega_c\right)^2}\right] B_x \sin p\omega_c t. \end{aligned} \quad (13)$$

3.2.3. Derivation of $M_z^{(2)}$, the solution for M_z of order $q = 2$

Substituting $M_y^{(1)}$ of Eq. (13) into Eq. (2b), when $\omega_c \gg \frac{1}{\tau_1}$, the modulation part in Eq. (13) has little contribution in Eq. (2b) and can be neglected. Hence, we can only substitute the DC term in Eq. (13) into Eq. (2b)

$$\frac{\mathrm{d}M_z^{(2)}}{\mathrm{d}t} = \frac{\left[M_0 - M_z^{(0)} \tau_1 \tau_2 \gamma^2 B_x^2 \cdot J\right] - M_z^{(2)}}{\tau_1}, \quad (14a)$$

where

$$J = \sum_{n=-\infty}^{n=+\infty} \frac{J_n^2\left(\frac{\omega_1}{\omega_c}\right)}{1+\tau_2^2\left(\omega_0+n\omega_c\right)^2}. \quad (14b)$$

We consider the steady-state solution, setting Eq. (14a) equal to zero and we obtain

$$M_z^{(2)} = M_0 - M_z^{(0)} \tau_1 \tau_2 \gamma^2 B_x^2 \cdot J. \quad (15)$$

Therefore, it can be seen that it should be satisfied so that

$$\tau_1 \tau_2 \gamma^2 B_x^2 \cdot J < 1. \quad (16)$$

3.2.4. Derivation of $M_+^{(3)}$, the solution for M_+ of order $q = 3$

Substituting $M_z^{(2)}$ of Eq. (15) into Eq. (2a), by the same method as in Subsection 3.2.2, we can obtain the analytical solution for $M_+^{(3)}$

$$M_+^{(3)} = \mathrm{i} M_z^{(2)} \tau_2 \gamma B_x \sum_{p=-\infty}^{+\infty} \sum_{n=-\infty}^{+\infty} \frac{J_n\left(\frac{\omega_1}{\omega_c}\right) J_{n-p}\left(\frac{\omega_1}{\omega_c}\right)}{1+\mathrm{i}\tau_2\left(\gamma B_0 + n\omega_c\right)} \mathrm{e}^{\mathrm{i}p\omega_c t}. \quad (17)$$

Then, we can obtain $M_y^{(3)} = \mathrm{Im}\left[M_+^{(3)}\right]$:

$$M_y^{(3)} = M_z^{(2)} \tau_2 \gamma B_x \cdot J + \delta M_y^{(3)}, \quad (18)$$

where $\delta M_y^{(3)}$ denotes the modulation part of $M_y^{(3)}$ and has a similar expression to that in $M_y^{(1)}$ of Eq. (13).

3.2.5. Derivation of $M_z^{(4)}$, the solution for M_z of order $q = 4$

By the same method as in Subsection 3.2.3, substituting the DC term of $M_y^{(3)}$ in Eq. (18) into Eq. (2b), we have

$$\frac{\mathrm{d}M_z^{(4)}}{\mathrm{d}t} = \frac{\left[M_0 - M_z^{(2)} \tau_1 \tau_2 \gamma^2 B_x^2 \cdot J\right] - M_z^{(4)}}{\tau_1}. \quad (19)$$

We consider the steady-state solution, setting Eq. (19) equal to zero, and we obtain

$$M_z^{(4)} = M_0 - M_z^{(2)} \tau_1 \tau_2 \gamma^2 B_x^2 \cdot J. \quad (20)$$

According to Eqs. (20), (15) and (10), we can summarize that

$$M_z^{(2)} - M_z^{(0)} = \left[-\tau_1 \tau_2 \gamma^2 B_x^2 \cdot J\right] M_z^{(0)}, \quad (21)$$

$$\begin{aligned} M_z^{(4)} - M_z^{(2)} &= \left[-\tau_1 \tau_2 \gamma^2 B_x^2 \cdot J\right] \left(M_z^{(2)} - M_z^{(0)}\right) \\ &= \left[-\tau_1 \tau_2 \gamma^2 B_x^2 \cdot J\right]^2 M_z^{(0)}, \end{aligned} \quad (22)$$

$$\cdots$$

$$\begin{aligned} M_z^{(2k)} - M_z^{(2k-2)} &= \left[-\tau_1 \tau_2 \gamma^2 B_x^2 \cdot J\right] \left(M_z^{(2k-2)} - M_z^{(2k-4)}\right) \\ &= \left[-\tau_1 \tau_2 \gamma^2 B_x^2 \cdot J\right]^k M_z^{(0)}. \end{aligned} \quad (23)$$

Adding up Eqs. (21)–(23), we have

$$\begin{aligned} M_z^{(q=2k)} = {} & M_z^{(0)} + \left[-\tau_1 \tau_2 \gamma^2 B_x^2 \cdot J\right] M_z^{(0)} + \left[-\tau_1 \tau_2 \gamma^2 B_x^2 \cdot J\right]^2 M_z^{(0)} \\ & + \cdots + \left[-\tau_1 \tau_2 \gamma^2 B_x^2 \cdot J\right]^k M_z^{(0)}. \end{aligned} \quad (24)$$

Combining Eqs. (24) and (8b), we recall the condition $\tau_1 \tau_2 \gamma^2 B_x^2 \cdot J < 1$ in Eq. (16) and can obtain the approximated analytical solution for M_z of order $q = \infty$

$$\begin{aligned} M_z &= M_0 \lim_{k\to\infty} \left\{\frac{1-\left[-\tau_1 \tau_2 \gamma^2 B_x^2 \cdot J\right]^k}{1+\tau_1 \tau_2 \gamma^2 B_x^2 \cdot J}\right\} \\ &= \frac{M_0}{1+\tau_1 \tau_2 \gamma^2 B_x^2 \cdot J}. \end{aligned} \quad (25)$$

Then, we consider the case when $\tau_1 \tau_2 \gamma^2 B_x^2 \cdot J \geq 1$. We suppose that the steady-state solution of M_z is still given by Eq. (25). Substituting Eq. (25) into Eq. (2a), by the same method as in Subsection 3.2.2, we can obtain the analytical solution of M_y

$$M_y = \frac{M_0 \tau_2 \gamma B_x}{1+\tau_1 \tau_2 \gamma^2 B_x^2 \cdot J} \cdot J + \delta M_y, \quad (26)$$

where δM_y is the modulation part.

By the same method as in Subsection 3.2.3, substituting the DC term of M_y in Eq. (26) and M_z in Eq. (25) into Eq. (2b), we find that the resulting equation satisfies the conditions for a steady-state solution exactly,

$$\frac{\mathrm{d}M_z}{\mathrm{d}t} = 0. \quad (27)$$

Therefore, we are assured that Eq. (25) can be used as an approximate steady-state solution for M_z under the condition $\tau_1\tau_2\gamma^2B_x^2\cdot J \geq 1$. Finally, we obtain the general analytical model describing the relationship between M_z and B_x. It can be seen that when the amplitude of the measured magnetic fields B_x is large enough, the value of M_z will be significantly influenced by B_x; as the amplitude of B_x increases, the value of M_z decreases.

Substituting the solution for M_z of Eq. (25) into Eq. (2a), we can solve the equation and obtain the magnetometer signal M_x and the modulation part δM_x which is given by

$$\begin{aligned}\delta M_x = {} & M_0\tau_2\gamma\times\frac{1}{1+\tau_1\tau_2\gamma^2B_x^2\cdot J}\\ & \times\sum_{p=1}^{\infty}\left[\sum_{n=-\infty}^{+\infty}\frac{\beta_{np}^-}{1+\tau_2^2\left(\omega_0+n\omega_c\right)^2}\right]B_x\sin p\omega_c t\\ & +\left[\sum_{n=-\infty}^{+\infty}\frac{\beta_{np}^+\cdot\tau_2\left(\omega_0+n\omega_c\right)}{1+\tau_2^2\left(\omega_0+n\omega_c\right)^2}\right]B_x\cos p\omega_c t. \qquad (28)\end{aligned}$$

Comparing Eq. (28) and Eq. (7a), we have modified the fundamental model of Eq. (7a) by adding the modification factor $\frac{1}{1+\tau_1\tau_2\gamma^2B_x^2\cdot J}$. Equation (28) shows that the magnetometer signal is related to the transverse magnetic fields by the magnetometer-response function $f(B_x)=\frac{B_x}{1+\tau_1\tau_2\gamma^2B_x^2\cdot J}$. We can analyze the derivatives of function $f(B_x)$ with respect to the parameter B_x, which is the slope S of the magnetometer-response curve $f(B_x)\sim B_x$,

$$S=\frac{\mathrm{d}}{\mathrm{d}B_x}\left[\frac{B_x}{1+\tau_1\tau_2\gamma^2B_x^2\cdot J}\right]=\frac{1-\tau_1\tau_2\gamma^2B_x^2\cdot J}{\left[1+\tau_1\tau_2\gamma^2B_x^2\cdot J\right]^2}. \qquad (29)$$

When the amplitude of B_x is very small that $\tau_1\tau_2\gamma^2B_x^2\cdot J\ll 1$, the slope $S\approx 1$, indicating our desirable linear-measurement range of the magnetometer. As the amplitude of B_x increases, the slope S decreases but is still positive, indicating that the linear-response performance of the magnetometer gradually deteriorates. When the amplitude of B_x increases to be at the turning point where $\tau_1\tau_2\gamma^2B_x^2\cdot J=1$, the slope $S=0$, indicating the maximum effective measuring range of the magnetometer; as the amplitude of B_x continues to increase, slope S becomes negative and the curve moves downwards, where the magnetometer completely fails to work .

According to Eq. (28), the linear-measurement characteristics of the magnetometer have relationships with these working conditions: the amplitude and frequency of the carrier field determining the value of J, longitudinal spin relaxation time τ_1 and transverse spin relaxation time τ_2; the carrier fields can also influence the spin relaxation time.[19] In order to minimize the influence of a large B_x on the value of the modification factor, the smaller the values of J and $\tau_1\tau_2$, the higher the linear-response capacity of the magnetometer.

4. Numerical simulation and discussion

To demonstrate the validity of our theoretical modification of Eq. (28), we carry out numerical simulation according to Bloch Eq. (1) with our own simulation system constructed by LabVIEW software. The block diagram of the simulation system is shown in Fig. 2. The values of the parameters can be set by inputting to Bloch Equation Solver in the simulation system, incorporating the magnetic fields applied along three axes, the longitudinal and transverse spin relaxation time. The Bloch Equation Solver outputs the values of M_x, M_y and M_z of alkali spins. After being amplified in the gain module, the M_x signal is multiplied by the reference signal of longitudinal carrier fields with a certain phase delay and then processed in the low-pass filter to generate the in-phase or quadrature demodulation results.

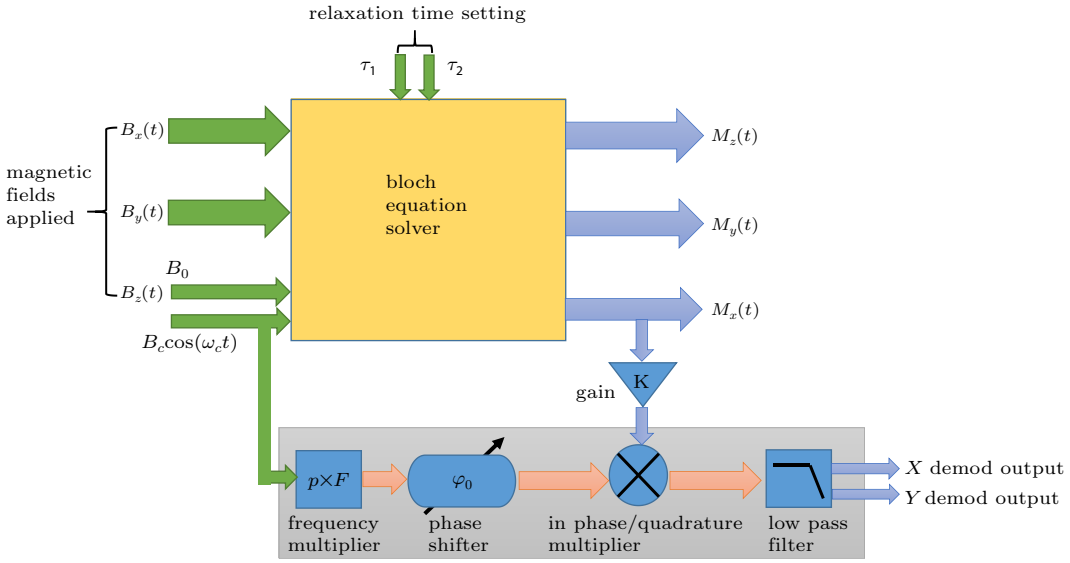


Fig. 2. Block diagram of the simulation system.

The main parameters are as follows: $B_0 = 10$ μT, $\gamma = 2\pi \times 3499$ Hz/μT (the alkali metal is ^{133}Cs). We consider quadrature demodulating the first ($p = 1$) harmonic of the magnetometer signal M_x and other parameters for different design examples are given in the specific simulations:

4.1. The n = –1 modulation for different amplitudes of the carrier magnetic field

We set $\omega_c = \omega_0 = \gamma B_0$; $\tau_1 = 200$ μs, $\tau_2 = 100$ μs. In Eq. (28), as $\omega_c \gg 1/\tau_2$, and the resonance condition $\omega_0 - \omega_c = 0$ is satisfied for certain parametric modulation, we can only consider the resonances at n near -1. The condition that $\omega_c \gg 1/\tau_1$ is also satisfied. The parameter of B_c will be assigned different values. We measure the magnetometer signal response and longitudinal magnetization as the amplitude of the static field B_x is scanned.

The simulation results and corresponding approximate results of the modified analytic solution are shown in Fig. 3. It is clear that the theoretical results agree well with the simulation results.

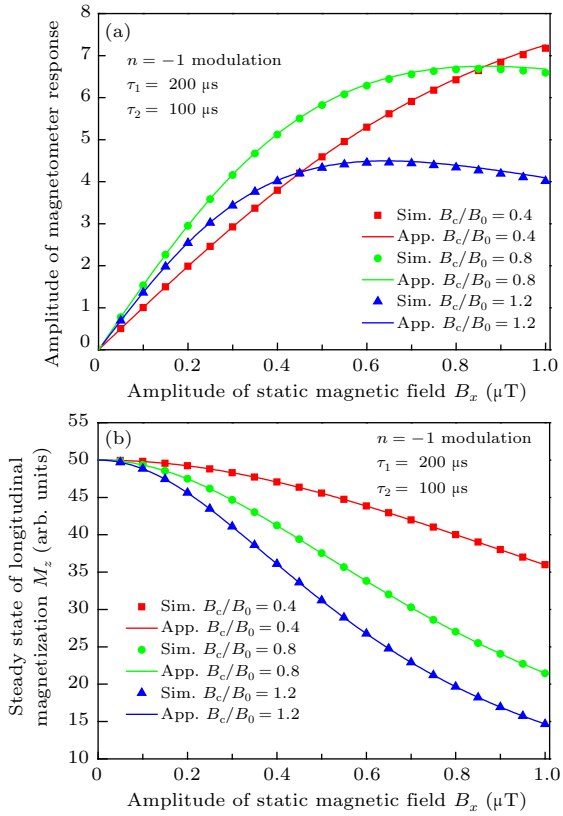


Fig. 3. Magnetometer output for $n = -1$ modulation under different conditions of amplitudes of the carrier magnetic field: (a) the amplitude of magnetometer response; (b) the steady state of longitudinal magnetization M_z. "Sim." and "App." in the figure denote numerical simulation and approximate analytical results, respectively.

According to Eq. (28), assuming that the $n \neq -1$ terms can be neglected, we have

$$\delta M_{x,\sin}^{p=1} \approx M_0 \tau_2 \gamma \left\{ J_1\left(\frac{B_c}{B_0}\right)\left[J_2\left(\frac{B_c}{B_0}\right) - J_0\left(\frac{B_c}{B_0}\right)\right]\right\} \times \frac{1}{1+\tau_1\tau_2\gamma^2 B_x^2 \cdot J_1^2\left(\frac{B_c}{B_0}\right)} \times B_x \sin\omega_c t. \quad (30)$$

In Eq. (30), the signal magnitude is proportional to the value of $\left|J_1\left(\frac{B_c}{B_0}\right)\left[J_2\left(\frac{B_c}{B_0}\right) - J_0\left(\frac{B_c}{B_0}\right)\right]\right|$ and the linear-measurement performance is dependent on the value of $J_1^2\left(\frac{B_c}{B_0}\right)$. In order to maximize the signal magnitude, the value of $\left|J_1\left(\frac{B_c}{B_0}\right)\left[J_2\left(\frac{B_c}{B_0}\right) - J_0\left(\frac{B_c}{B_0}\right)\right]\right|$ should be as large as possible. In order to maximize the linear-response capacity of the magnetometer, we should minimize the influence of a large B_x on the value of the modification factor. Therefore, the value of $J_1^2\left(\frac{B_c}{B_0}\right)$ should be as small as possible. The functions $\left|J_1\left(\frac{B_c}{B_0}\right)\left[J_2\left(\frac{B_c}{B_0}\right) - J_0\left(\frac{B_c}{B_0}\right)\right]\right|$ and $J_1^2\left(\frac{B_c}{B_0}\right)$ with respect to the argument B_c/B_0 are plotted in Fig. 4.

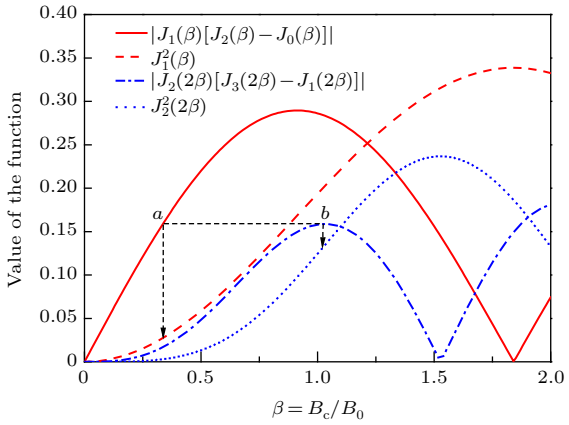


Fig. 4. Functions combined according to Eqs. (30) and (32) plotted against $\beta = B_c/B_0$.

Assuming that the actual magnetic fields to be measured are B_x, which should be within the effective measuring range (determined by $\tau_1\tau_2\gamma^2 B_x^2 \cdot J_1^2(B_c/B_0) < 1$) of the magnetometer, the corresponding practical experimental measuring results based on the fundamental model of Eq. (7a) are B_x'. According to Eq. (30), the relative error (REr) of this measurement can be expressed as

$$\mathrm{REr} = \frac{B_x - B_x'}{B_x} = 1 - \frac{1}{1+\tau_1\tau_2\gamma^2 B_x^2 \cdot J_1^2\left(\frac{B_c}{B_0}\right)}. \quad (31)$$

It can be seen that the relative error depends on the relaxation time $\tau_1\tau_2$, the actual magnetic fields to be measured B_x, and the z-axis magnetic fields B_c/B_0. The larger the $\tau_1\tau_2$ and B_x, the larger the measurement error. According to Eq. (31), we can plot the curves that the relative errors vary with B_c/B_0 in the range of (0, 0.9), under different conditions of amplitudes of the actual magnetic fields B_x, as shown in Fig. 5.

Figure 5 clearly indicates that when B_c/B_0 is greater than a certain value, the error will exceed a certain upper limit and we should apply the modified analytical model to modify the measurement results, in order to meet the required accuracy for the magnetometer.

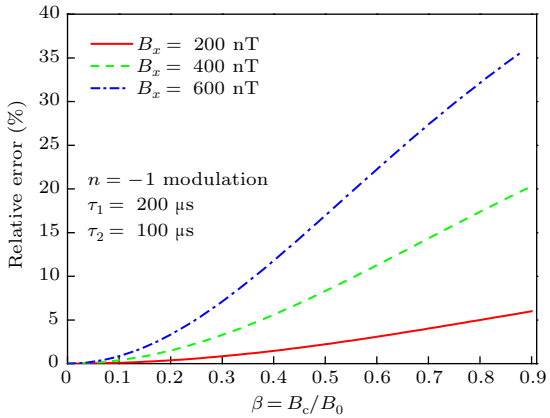


Fig. 5. Relative errors vary with B_c/B_0 under different conditions of amplitudes of the actual magnetic fields B_x.

4.2. The n = –2 modulation for different amplitudes of the carrier magnetic field

We set $\omega_c = \frac{1}{2}\omega_0 = \frac{1}{2}\gamma B_0$; $\tau_1 = 200$ μs, $\tau_2 = 100$ μs. In Eq. (28), as $\omega_c \gg 1/\tau_2$, and the resonance condition $\omega_0 - 2\omega_c = 0$ is satisfied for certain parametric modulation, we can only consider the resonances at n near -2. The condition that $\omega_c \gg 1/\tau_1$ is also satisfied. The parameter of B_c will be assigned different values. We measure the magnetometer signal response and longitudinal magnetization as the amplitude of the static field B_x is scanned. The simulation results and corresponding approximate results of the modified analytic solution are shown in Fig. 6. It is clear that the theoretical results agree well with the simulation results.

According to Eq. (28), assuming that the $n \neq -2$ terms can be neglected, we have

$$\delta M_{x,\sin}^{p=1} \approx M_0 \tau_2 \gamma \left\{ J_2\left(\frac{2B_c}{B_0}\right)\left[J_3\left(\frac{2B_c}{B_0}\right) - J_1\left(\frac{2B_c}{B_0}\right)\right]\right\} \times \frac{1}{1+\tau_1\tau_2\gamma^2 B_x^2 \cdot J_2^2\left(\frac{2B_c}{B_0}\right)} \times B_x \sin\omega_c t. \quad (32)$$

In Eq. (32), the signal magnitude is proportional to the value of $\left|J_2\left(\frac{2B_c}{B_0}\right)\left[J_3\left(\frac{2B_c}{B_0}\right) - J_1\left(\frac{2B_c}{B_0}\right)\right]\right|$ and the linear-measurement performance is dependent on the value of $J_2^2\left(\frac{2B_c}{B_0}\right)$. In order to maximize the signal magnitude, the value of $\left|J_2\left(\frac{2B_c}{B_0}\right)\left[J_3\left(\frac{2B_c}{B_0}\right) - J_1\left(\frac{2B_c}{B_0}\right)\right]\right|$ should be as large as possible. In order to maximize the linear-response capacity of the magnetometer, the value of $J_2^2\left(\frac{2B_c}{B_0}\right)$ should be as small as possible. The functions $\left|J_2\left(\frac{2B_c}{B_0}\right)\left[J_3\left(\frac{2B_c}{B_0}\right) - J_1\left(\frac{2B_c}{B_0}\right)\right]\right|$ and $J_2^2\left(\frac{2B_c}{B_0}\right)$ with respect to the argument $\frac{B_c}{B_0}$ are plotted in Fig. 4.

In Fig. 4, within the range of $\frac{B_c}{B_0}$ is (0, 2), working point b is about the maximum point on the curve $\left|J_2\left(\frac{2B_c}{B_0}\right)\left[J_3\left(\frac{2B_c}{B_0}\right) - J_1\left(\frac{2B_c}{B_0}\right)\right]\right|$ and working point a on the curve $\left|J_1\left(\frac{B_c}{B_0}\right)\left[J_2\left(\frac{B_c}{B_0}\right) - J_0\left(\frac{B_c}{B_0}\right)\right]\right|$ has the same value as working point b. However, considering the linear-measurement capacity, point a on the curve $J_1^2\left(\frac{B_c}{B_0}\right)$ has much smaller value than point b on the curve $J_2^2\left(\frac{2B_c}{B_0}\right)$. On the other hand, since providing a stable high-amplitude modulation current into the coils is difficult for electronic devices in practice, we prefer working point a because it requires much smaller amplitude of carrier magnetic field B_c than that of working point b. Hence, for the case here, choosing $n = -1$ modulation is better for configuring this magnetometer.

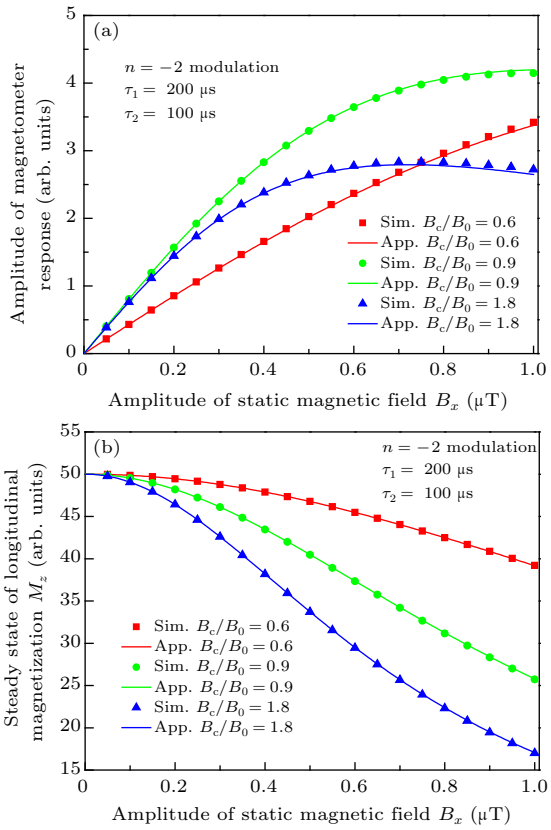


Fig. 6. Magnetometer output for $n = -2$ modulation under different conditions of amplitudes of the carrier magnetic field: (a) the amplitude of magnetometer response; (b) the steady state of longitudinal magnetization M_z. "Sim." and "App." in the figure denote numerical simulation and approximate analytical results, respectively.

4.3. The n = –1 modulation for different longitudinal and transverse relaxation time

Setting $\omega_c = \omega_0 = \gamma B_0$; $B_c/B_0 = 1.5$; the parameters of τ_1 and τ_2 will be assigned different values and the condition that $\omega_c \gg 1/\tau_1$, $\omega_c \gg 1/\tau_2$ should be satisfied for all examples. We measure the magnetometer signal response and longitudinal magnetization as the amplitude of the static field B_x is scanned.

The simulation results and corresponding approximate results of the modified analytic solution are shown in Fig. 7. It is clear that the theoretical results agree well with the simulation results. According to Eq. (30) and Fig. 7, it can be seen that the smaller the spin relaxation time, the smaller the signal magnitude but the higher the linear-measurement capacity. When choosing proper parameters for the carrier magnetic fields and spin relaxation time, we should consider the fact that B_c will

also influence the spin relaxation.[19] Furthermore, if the precise values of τ_2 and other working conditions are known, we can obtain the value of τ_1 by fitting the magnetometer response curve with our modified theoretical model, which provides a new method to measure the longitudinal spin relaxation time τ_1.

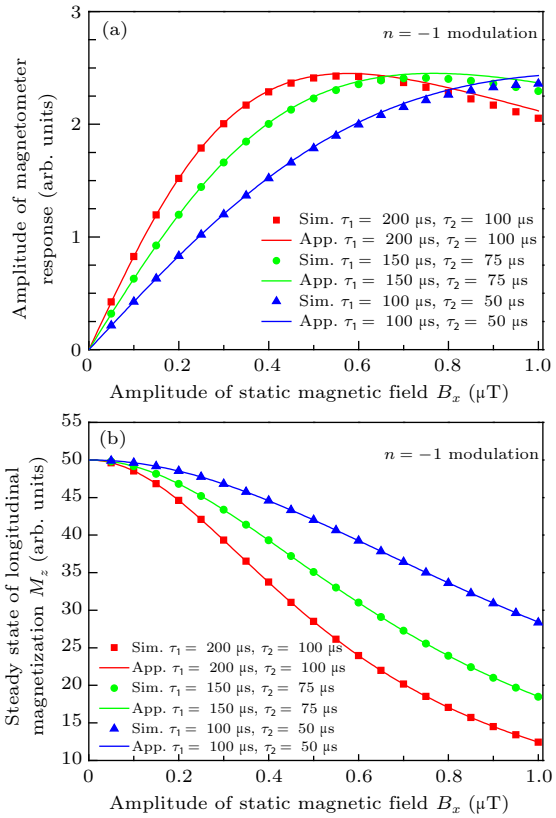


Fig. 7. Magnetometer output for $n = -1$ modulation under different conditions of longitudinal and transverse relaxation time: (a) the amplitude of magnetometer response; (b) the steady state of longitudinal magnetization M_z. "Sim." and "App." in the figure denote numerical simulation and approximate analytical results, respectively.

4.4. The $n = -1$ modulation for different angular frequency of the rotation field

As already noted in the beginning, NMR detection in a spin-exchange NMR oscillator can be realized by using the alkali atoms as an integrated magnetometer. In NMR oscillators, by applying a "drive" field that rotates in the same direction as the nuclear spins and at a frequency close to their NMR frequency, the nuclear spins can be induced to precess about the z-axis. Assuming that B_1 rotates about the z-axis with amplitude B_1 and angular frequency ω_r, the components of the rotation field along x-axis and y-axis are

$$B_x = B_1 \cos(\omega_r t), \tag{33a}$$

$$B_y = B_1 \sin(\omega_r t). \tag{33b}$$

Then, a rotating coordinate system $x'y'z$ is introduced to simplify the analysis, as shown in Fig. 8. The rotating coordinates are defined by the condition that x'-axis rotates in phase with B_1 about the z-axis and y'-axis rotates in quadrature. The rotation field is the equivalent of a static field in the rotating coordinate system.

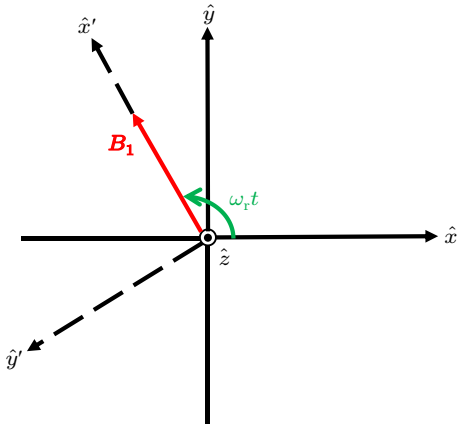


Fig. 8. xyz: laboratory coordinate system and $x'y'z$: rotating coordinate system.

Therefore, we have the relations

$$M_x = M_{x'}\cos(\omega_r t) - M_{y'}\sin(\omega_r t), \tag{34a}$$

$$M_y = M_{x'}\sin(\omega_r t) + M_{y'}\cos(\omega_r t). \tag{34b}$$

Substituting Eqs. (33a) and (33b) into Bloch-like Eq. (1), and using Eqs. (34a) and (34b), the following equations are obtained in the rotating coordinate frame:

$$\frac{\mathrm{d}M_{+'}}{\mathrm{d}t} + \left\{\frac{1}{\tau_2} + \mathrm{i}\left[\omega_0 + \omega_r + \omega_1\cos(\omega_c t)\right]\right\} M_{+'} = \mathrm{i}M_z\gamma B_1, \tag{35a}$$

$$\frac{\mathrm{d}M_z}{\mathrm{d}t} = \frac{\left[M_0 - \tau_1\gamma B_1 M_{y'}\right] - M_z}{\tau_1}, \tag{35b}$$

where $M_{+'} = M_{x'} + \mathrm{i}M_{y'}$.

Comparing Eqs. (35a) and (35b) and Eqs. (2a) and (2b), using the same method to derive the solutions to Eqs. (2a) and (2b), we can obtain the solutions to Eqs. (35a) and (35b). Considering the quadrature demodulation at harmonic $p\omega_c$, we have

$$M_z = M_0 \cdot \frac{1}{1 + \tau_1\tau_2\gamma^2 B_1^2 \cdot J_r}, \tag{36a}$$

$$\delta M^p_{x',\sin} = M_0\tau_2\gamma a_1 \cdot \frac{1}{1 + \tau_1\tau_2\gamma^2 B_1^2 \cdot J_r} B_1 \sin p\omega_c t, \tag{36b}$$

$$\delta M^p_{y',\sin} = M_0\tau_2\gamma b_1 \cdot \frac{1}{1 + \tau_1\tau_2\gamma^2 B_1^2 \cdot J_r} B_1 \sin p\omega_c t, \tag{36c}$$

where

$$a_1 = \sum\nolimits_{n=-\infty}^{+\infty} \frac{\beta^-_{np}}{1 + \tau_2^2(\omega_0 + \omega_r + n\omega_c)^2}, \tag{36d}$$

$$b_1 = \sum\nolimits_{n=-\infty}^{+\infty} \frac{-\beta^-_{np}\cdot\tau_2(\omega_0 + \omega_r + n\omega_c)}{1 + \tau_2^2(\omega_0 + \omega_r + n\omega_c)^2}, \tag{36e}$$

$$J_r = \sum_{n=-\infty}^{n=+\infty} \frac{J_n^2\left(\frac{\omega_1}{\omega_c}\right)}{1 + \tau_2^2(\omega_0 + \omega_r + n\omega_c)^2}. \tag{36f}$$

According to Eq. (34a), we can obtain the magnetometer signal

$$\begin{aligned}\delta M^{p}_{x,\sin} &= \delta M^{p}_{x',\sin}\cos(\omega_{\rm r}t) - \delta M^{p}_{y',\sin}\sin(\omega_{\rm r}t)\\ &= M_0\tau_2\gamma\times\frac{1}{1+\tau_1\tau_2\gamma^2B_1^2\cdot J_{\rm r}}\\ &\quad\times c_1B_1\cos(\omega_{\rm r}t+\varphi)\sin p\omega_{\rm c}t,\end{aligned}\tag{37}$$

where $c_1=\sqrt{a_1^2+b_1^2}$, $\cos\varphi=a_1/c_1$, and $\sin\varphi=b_1/c_1$.

Equation (37) shows that the angular frequency $\omega_{\rm r}$ not only influences the amplitude-frequency response,[20] but the linear-measurement characteristics of the magnetometer when measuring the rotation field.

Then, we conduct the simulation experiments to verify the modified analytical model of Eq. (37). We consider the first ($p=1$) harmonics of the modulation and observe the $n=-1$ modulation, $\omega_{\rm c}=\omega_0=\gamma B_0$, and we set $B_{\rm c}/B_0=1.5$, $\tau_1=200$ μs, $\tau_2=100$ μs. As $\omega_{\rm r}\ll\omega_{\rm c}$, $\omega_{\rm c}\gg1/\tau_2$, we can only consider the resonances at n near -1. The condition that $\omega_{\rm c}\gg1/\tau_1$ is also satisfied. The parameter of $\omega_{\rm r}$ will be assigned different values. We measure the magnetometer signal response and longitudinal magnetization as the amplitude of the rotation field B_1 is scanned. The simulation results and corresponding approximate results of the modified analytical solution are shown in Fig. 9. It is clear that the theoretical results agree well with the simulation results.

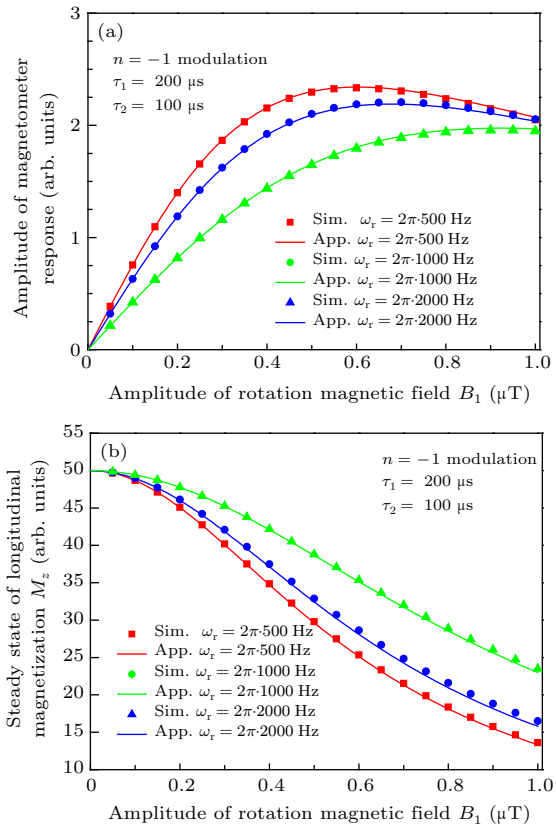


Fig. 9. Magnetometer output for $n=-1$ modulation under different conditions of angular frequency of the rotation field: (a) the amplitude of magnetometer response; (b) the steady state of longitudinal magnetization M_z. "Sim." and "App." in the figure denote numerical simulation and approximate analytical results, respectively.

Assuming that the $n\neq-1$ terms can be neglected, we have

$$\begin{aligned}\delta M^{p=1}_{x,\sin} &\approx M_0\tau_2\gamma\times J_1\left(\frac{\omega_1}{\omega_{\rm c}}\right)\left[J_2\left(\frac{\omega_1}{\omega_{\rm c}}\right)-J_0\left(\frac{\omega_1}{\omega_{\rm c}}\right)\right]\\ &\quad\times\frac{1}{1+\frac{\tau_1\tau_2\gamma^2B_1^2J_1^2\left(\frac{\omega_1}{\omega_{\rm c}}\right)}{1+\tau_2^2\omega_{\rm r}^2}}\times\frac{1}{\sqrt{1+\tau_2^2\omega_{\rm r}^2}}\\ &\quad\times B_1\cos(\omega_{\rm r}t+\varphi)\sin\omega_{\rm c}t,\end{aligned}\tag{38}$$

where $\cos\varphi=1/\sqrt{1+\tau_2^2\omega_{\rm r}^2}$ and $\sin\varphi=-\tau_2\omega_{\rm r}/\sqrt{1+\tau_2^2\omega_{\rm r}^2}$.

Combining Eq. (38) and Fig. 9, it can be clearly seen that the higher the angular frequency $\omega_{\rm r}$ of the rotation field, the smaller the signal magnitude but the higher the linear-measurement capacity of the magnetometer.

5. Conclusion

In summary, for the AMA magnetometer employing longitudinal carrier field, the amplitude of the magnetometer response is not proportional to the measured magnetic fields B_x when B_x is large, because the longitudinal magnetization M_z will be influenced by and vary with B_x. By theoretical derivation using the perturbation-iteration method, we present a modified theoretical model to more definitely analyze the practical linear-response characteristics of the magnetometer, which are determined by different working conditions. For the amplitude $B_{\rm c}$ and frequency $\omega_{\rm c}$ of the carrier field, the spin relaxation time τ_1 and τ_2, and the rotation frequency $\omega_{\rm r}$ of the measured transverse fields, the smaller the values of $|J_n(nB_{\rm c}/B_0)|$ (when $\omega_{\rm c}=\omega_0/n$) and $\tau_1\tau_2$, and the higher the rotation frequency $\omega_{\rm r}$, leading to higher linear-response capacity of the magnetometer. The larger amplitudes of the actual magnetic fields B_x to be measured, the larger the measurement error based on the existing fundamental model.

Hence, we can use this modified model to modify the measurement results to obtain more accurate values of the actual B_x and to optimize the working conditions and choose proper system parameters to achieve the desired performance for practical magnetometer systems. This modified theoretical model to describe the linear-response curves also provides a new method to measure the longitudinal relaxation time τ_1 for the alkali metal magnetometer.

References

[1] Budker D and Romalis M V 2007 *Nat. Phys.* **3** 227
[2] Seltzer S J 2008 *Developments in Alkali-metal Atomic Magnetometry* (Ph. D. Dissertation) (New Jersey: Princeton University)
[3] Bison G, Wynands R and Weis A 2003 *Appl. Phys. B* **76** 325
[4] Xu S, Yashchuk V V, Donaldson M H, Rochester S M, Budker D and Pines A 2006 *Proc. Natl. Acad. Sci. USA* **103** 12668

[5] Brown J M, Smullin S J, Kornack T W and Romalis M V 2010 *Phys. Rev. Lett.* **105** 151604
[6] Savukov I M and Romalis M V 2005 *Phys. Rev. Lett.* **94** 123001
[7] Cohen-Tannoudji C, Dupont-Roc J, Haroche S and Laloë F 1970 *Rev. Phys. Appl.* **5** 95
[8] Cohen-Tannoudji C, Dupont-Roc J, Haroche S and Laloë F 1969 *Phys. Rev. Lett.* **22** 758
[9] Grover B C 1978 *Phys. Rev. Lett.* **40** 391
[10] Volk C H, Kwon T M and Mark J G 1980 *Phys. Rev. A* **21** 1549
[11] Kanegsberg E 1978 *Proc. SPIE* **157** 73
[12] Eklund E J 2008 *Microgyroscope based on spin-polarized nuclei* (Ph.D. Dissertation) (California: University of California, Irvine)
[13] Ding Z, Yuan J, Luo H and Long X 2017 *Chin. Phys. B* **26** 093301
[14] Li Z, Wakai R T and Walker T G 2006 *Appl. Phys. Lett.* **89** 134105
[15] Ding Z, Yuan J, Lu G, Li Y and Long X 2017 *IEEE Photonics Journal* **9** 5300209
[16] Happer W 1972 *Rev. Mod. Phys.* **44** 169
[17] Zhang D W, Xu Z Y, Zhou M and Xu X Y 2017 *Chin. Phys. B* **26** 023201
[18] Fu Y and Yuan J 2019 *Chin. Phys. B* **28** 098504
[19] Savukov I M and Romalis M V 2005 *Phys. Rev. A* **71** 023405
[20] Chen C, Jiang Q, Wang Z, Zhang Y, Luo H and Yang K 2020 *AIP Adv.* **10** 065303